Supplemental Information for:

The Effect of Nanoparticle Size on Calendar and Cycle Lifetimes of Silicon Anode Lithium-Ion Batteries

Juliane I. Preimesberger,[1] Francois L. E. Usseglio-Viretta,[2] Ankit Verma,[2] Avtar Singh,[2] Andrew M. Colclasure,[2] Patrick Walker,[1] Glenn Teeter,[1] Gregory F. Pach,[1] John Westgard,[1] Fernando Urias-Cordero,[1] Nathan R. Neale,[3,4] Jaclyn E. Coyle,[1,*] G. Michael Carroll[1,*]

1. *Materials Sciences Center, National Renewable Energy Laboratory, 15013 Denver West Parkway, Golden, Colorado 80401, United States*
2. *Energy Conversion and Storage Systems Center, National Renewable Energy Laboratory, Golden, Colorado 80401, United States*
3. *Chemistry and Nanoscience Center, National Renewable Energy Laboratory, 15013 Denver West Parkway, Golden, Colorado 80401, United States*
4. *Renewable and Sustainable Energy Institute, University of Colorado Boulder, Boulder, Colorado 80309, United States*

**Corresponding Author. Email Mike.Carroll@nrel.gov, Jaclyn.Coyl@nrel.gov*

Extended Methods:

Using a custom nonthermal RF-enhanced plasma reactor, PECVD spherical silicon nanoparticles (Si NPs) were generated for this study [1-4]. A summary of the growth conditions for each particle is shown in Table S1. The smaller particles require longer growth times, which is a consideration for any scale-up production (and another reason why the smallest 3 and 4 nm NPs may not be the optimal choice). Note that the 6 nm particle was made in a larger batch, which is why its run time was longer and other growth parameters are different from the other small NPs.

The major factors that control particle size are the pressure of the system, the gas flow rates, and the ratio of silane to hydrogen. Higher silane allows for more opportunities for Si-Si collisions (to form a particle), whereas higher hydrogen occupies surface coverage, closing the ability for more Si to accumulate before exiting the plasma. Effectively, more available Si sites will grow larger particles. Additionally, the toroidal injection of more silane into the middle of the plasma, where energy is too high for hydrogen to stay on the surface, can allow for particles to grow quite large.

Particle size was confirmed by X-ray powder diffraction measurements, where it was assumed the particles were single crystals, so the crystallite size (using Rietveld refinement), is the size of the full particle. Figure S1 plots the XRD results. The change in peak width denotes a change in crystallite size (wider peaks mean smaller crystallites).

Particles were surface-coated with allyloxy (poly)ethylene oxide (PEO), where the ligand length was chosen such that the oligmer coating-to-particle weight ratio was approximately 20%. Table S2 reports the oligmer length chosen for each particle. Also reported is the amount of *N*-Methyl pyrrolidone (NMP) added to suspend the coated particles in a slurry (smaller particles tend

to gel so more NMP was added to prevent this). The resulting solids loading of each slurry ranged

Table S1: PECVD particle growth parameters.

Particle diameter from XRD (nm)	**Pressure (Torr)**	**Tube**	**Forward Power (Wf)**	SiH_4 **(sccm)**	H_2 **(sccm)**	**Ar (sccm)**	**He (sccm)**	**Run time (min)**	**Yield (g)**
3.1	3	¼" alumina	90	3	90	30	27	358	0.2
4.2	3	¼" alumina	90	3	60	60	27	243	0.18
5.9	3	1" alumina	250	20	250	20	0	818	12.1
7.8	3	¼" alumina	90	6	0	30	54	175	0.2
11.1	4.5	1" quartz toroidal	200	9; 30 toroidal	100	40	81	26	0.27
12.2	7.5	1" quartz toroidal	200	9; 30 toroidal	100	40	81	30	0.24
14.2	7.5	1" quartz toroidal	200	9; 30 toroidal	100	40	81	32	0.24
19.0	7.6	1" quartz toroidal	225	9; 120 toroidal	81	60	0	30	0.26
20.0	9.5	1" quartz toroidal	225	9; 120 toroidal	81	60	0	32	0.25
26.8	13	1" alumina toroidal	244	9; 120 toroidal	0	60	81	26	0.77

from 10-14%, due to the differences in oligmer-to-particle wt% ratios and additional NMP added. Coating and purifying the smallest particle sizes was challenging, as they did not disperse well in solution, possibly due to an incomplete coating of PEO. The synthesis procedure wasn't optimized for the smallest nanoparticles, which resulted in a lower surface hydride concentration, which affects the quality of the PEO coating. This was evident as it was harder to suspend the 3 and 4 nm particles in solution, as improper coating leaves kinetically accessible surface hydrides that react with slurry components; this could explain why the 3 and 4 nm electrodes performed so poorly compared to the others. One potential way to solve this would be to increase the oligmer-to-particle ratio for smaller nanoparticles. Regardless, as these smallest NPs both require longer growth times and are more challenging to process into electrodes, a choice of a slightly larger NP (6 nm) which does perform very well without additional processing seems the most feasible pathway towards

making this chemistry commercially-viable. Therefore, additional attempts to fix the surface coating of the 3 and 4 nm particles were not made for this study.

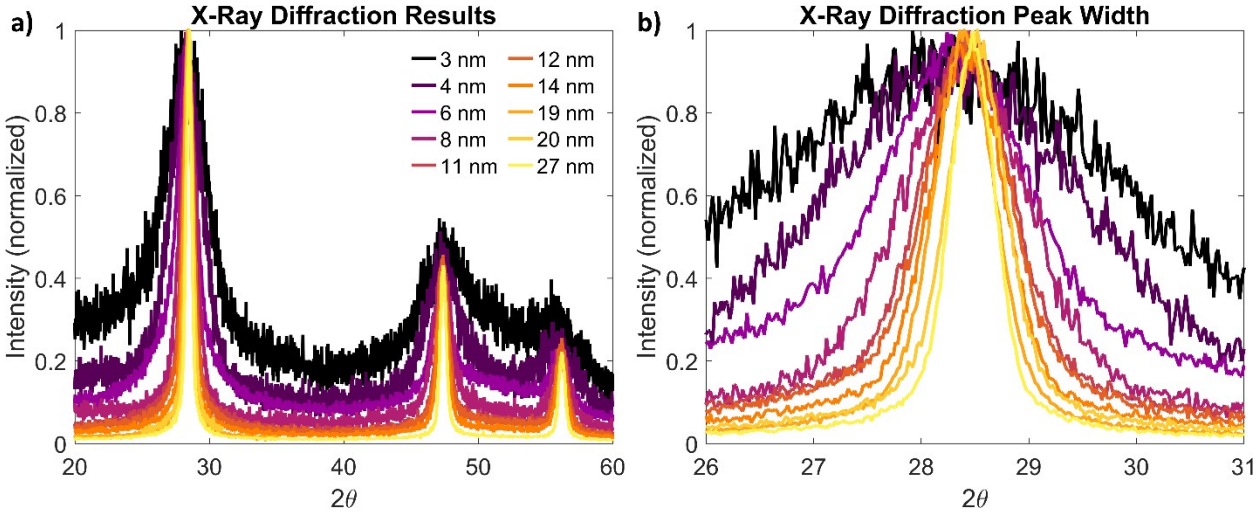

Figure S1: X-ray diffraction results for each particle size. a) Full diffraction pattern, normalized by maximum intensity. b) Zoomed-in diffraction pattern, showing how peak widths change with particle size.

Table S2: Average particle sizes, ligand length, ligand-to-particle wt%, and NMP wt% added to suspend the Si@PEO particles in the slurry, with the corresponding solids loading of the slurry.

Particle diameter (nm)	PEO oligmer length	Oligmer/particle (wt%)	NMP (wt%)	Solids loading (%)
3.1	n = 2	35.6	80	10.1
4.2	n = 2	29.0	80	10.8
5.9	n = 2	22.5	80	11.4
7.8	n = 2	18.0	80	11.9
11.1	n = 6-8	25.2	75	12.9
12.2	n = 6-8	23.5	80	11.3
14.2	n = 6-8	20.9	75	13.3
19.0	n = 6-8	16.5	75	13.8
20.0	n = 6-8	15.8	80	12.1
26.8	n = 6-8	12.3	75	14.2

Half Cell Electrochemical Results:

Half cells (vs. Li metal) were formed with three C/20 cycles. Nominal capacity for the half cells was set to the third C/20 discharge step. Half cells were then cycled at C/3 until 80% capacity was reached (voltage range 0.01 – 1.5 V, temperature 30 °C). Figure S2a and b plot the relative discharge capacity of half cells from the "lower loading" ($\sim 1\ mAh/cm^2$) and "higher loading" ($\sim 2\ mAh/cm^2$) electrodes. These results are consistent with the trend seen in the full cells (Figure 1), where the larger particles lose capacity faster. Interestingly, in half cells the 3 and 4 nm electrodes do not perform worse than the other small particle electrodes, presumably due to the differences

in overpotentials becoming irrelevant against lithium metal. Also, half cells experience an increase in capacity after formation, which likely indicates slow wetting or full lithiation of these electrodes. The number of cycles required to wet or fully utilize the electrode (Figure S2c) are higher for smaller particles, which might be due to electrode microstructure. Also plotted is the percentage of nominal capacity required to fully wet the electrodes; the smallest particle sizes require a higher supply of lithium inventory to fully wet than the larger particle sizes. The cycle lifetimes of the half cells for both electrode areal loadings are shown in Figure S2d, calculated as the number of cycles needed to reach 80% of the maximum capacity (i.e. after wetting). This wetting problem is less of an issue in the full cells mainly due to the limited lithium inventory in full cells. It might also be due to differences in formation, as the half cells did not undergo the 48 hour hold at the top of charge to fully utilize the electrode.

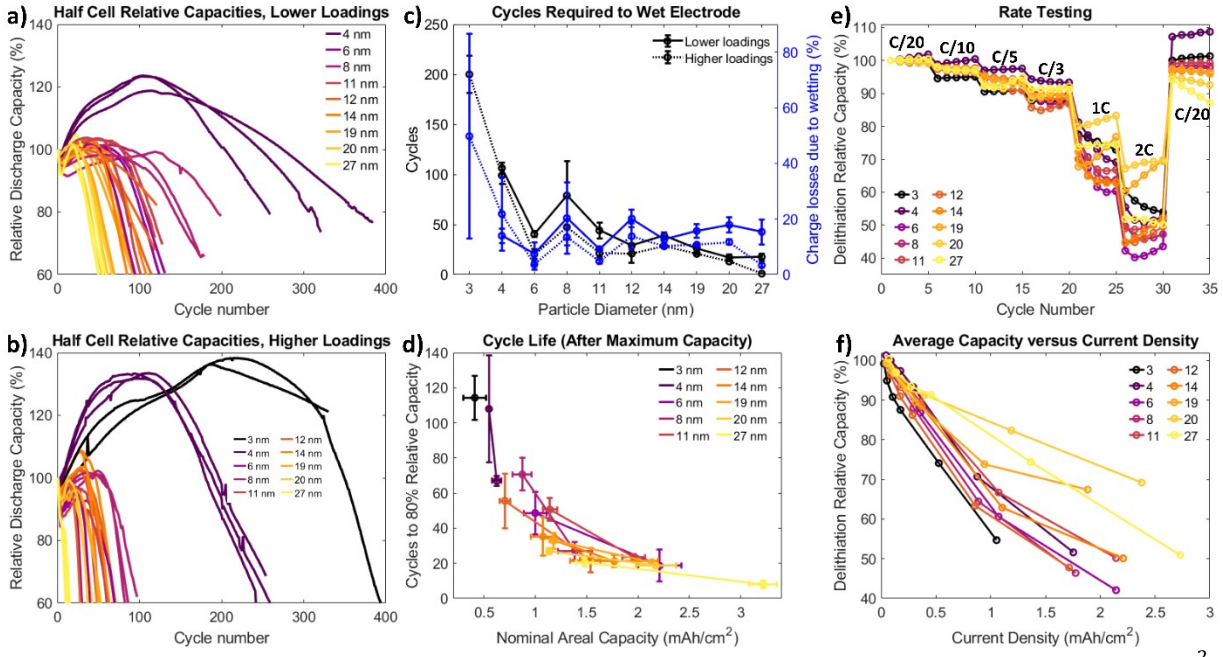

Figure S2: a) Half cell C/3 cycling for electrodes with areal loadings of around $0.5 - 1\ mAh/cm^2$. b) Half cell C/3 cycling for electrodes with areal loadings of around $1.5 - 2\ mAh/cm^2$. c) Number of cycles required to fully wet or utilize the electrode, calculated as number of cycles to reach maximum capacity. Also plotted is the total charge required to fully wet each electrode, which is the sum of all wetting cycles' charge losses. d) Cycle lifetimes of half cells, plotted against areal capacities, calculated as number of cycles to reach 80% capacity from the maximum capacity. e) Relative capacities of half cells during a rate performance test. f) Relative capacities versus applied current densities.

Rate performance tests were carried out using half cells. Rate performance testing half cells were cycled five times each at C/20, C/10, C/5, C/3, 1C, 2C, and C/20 following a formation of three C/20 cycles. Figure S2e and f plot the rate performances of each cell, showing no significant difference in rate capability except at higher current densities where larger-sized particle electrodes perform slightly better.

Following the rate performance tests, two C/100 cycles were performed. The lithiation and delithiation curves for the second C/100 cycle are shown in Figure S3a, and the voltage hysteresis ΔV versus capacity is plotted in Figure S3b. Voltage hysteresis is defined as the zero current voltage gap between lithiation and delithiation potentials [5, 6]. For intercalation-based lithium-ion battery electrodes, the equilibrium potential for lithiation and delithiation should merge as the electrodes reach the thermodynamic state at zero current where there are no reaction and transport overpotentials. However, silicon electrodes show a finite voltage hysteresis of greater than 200 mV [7]. Several causes of voltage hysteresis have been proposed in literature, including differing reaction pathways during charge and discharge, phases changes, and diffusion induced stress in silicon [6,8-11].

In PECVD silicon anodes, we can neglect the first two mechanisms as the lithium alloying reaction is the same during lithiation and delithiation, and the crystalline to amorphous transition occurs in the first lithiation, beyond which the silicon behaves as a single-phase material. Therefore, stress is hypothesized to be the primary mechanism for voltage hysteresis. Equilibrium potential in stressed state (U) is dependent on the stress-free equilibrium potential (U^0), surface pressure (p_s), Faraday's constant $F = 96485.33\ C/mol$, and molar volume of intercalated lithium ($\Omega_{Li} = 9cm^3/mol$) as follows [12]:

$$U = U^0 - \frac{\Omega_{Li} p_s}{F} \tag{1}$$

Consequently, the average stress state of the particle surface can be calculated as:

$$p_{s,avg} = \frac{|U - U^0|F}{\Omega_{Li}} = \frac{|V^{lith} - V^{delith}|F}{2\Omega_{Li}} = \frac{|V^{diff}|F}{2\Omega_{Li}} \tag{2}$$

Here, we use the convention that the particle surface stress is tensile (positive) during delithiation and compressive (negative) during lithiation with single phase diffusion of lithium into the particle [13]. The hysteresis between lithiation and delithiation was averaged over the middle third of the voltage window. A C/100 rate is used to mimic thermodynamic equilibrium and avoid any overpotential contributions from reaction and transport.

As shown in Figure S3c, the estimated stress in each electrode during a C/100 cycle is very similar, with the smallest particles experiencing slightly higher stresses. The GPa level stresses indicates there might be significant agglomeration of the silicon particles, which constrains the particles during volume expansion. This is consistent with the SEM images of these electrodes (Figure 3 and Figure S16) which show a very dense electrode structure.

Galvanostatic intermittent titration technique (GITT) was performed on the half cells after rate testing and the C/100 cycles. GITT can be used in half cells to estimate solid phase diffusivity of active electrode materials [14]. Figure S4a plots an example GITT voltage profile; there are 50 pulses each during lithiation and delithiation. A C/10 current is applied for 10 minutes followed by two hours of rest to allow for relaxation. The inset shows the current pulse profiles.

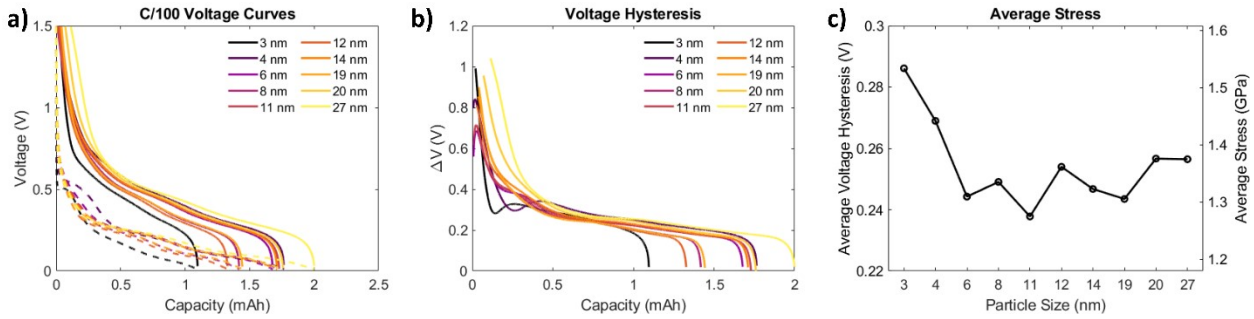

Figure S3: Calculation of stress state and results for each electrode. a) Voltage curves for a C/100 cycle in a half cell. Solid lines are delithiation and dashed lines are lithiation. b) Voltage hysteresis for each electrode at a C/100 rate. c) Voltage hysteresis, averaged over the middle third of the voltage window, and the corresponding calculated stress.

Diffusivity, D_s, can be computed using the standard Weppner-Huggins equation [15]:

$$D_s = \frac{4}{\pi}\left[\frac{IV_m}{FS}\right]^2\left[\frac{dU^0(x)/dx}{dV(t)/d\sqrt{t}}\right] \quad (3)$$

Where I is the current pulse value, V_m is the molar volume of silicon calculated using the molar mass and density of silicon ($V_m = MM_{Si}/\rho_{Si}$), F is Faraday's constant, $U^0(x)$ is the SOC (x) dependent open circuit potential, V is the voltage during the pulse, and t is the time during the pulse. The total electrochemically active area of the anode (S) is challenging to calculate in these dense electrodes, so diffusivity values are reported as D_sS^2. Lithiation and delithiation diffusivity values (averaged across SOC) are plotted in Figure S4b. There is no clear trend with particle size, and large variations between results might be more due to differences between electrode punches rather than differences inherent to the silicon NPs.

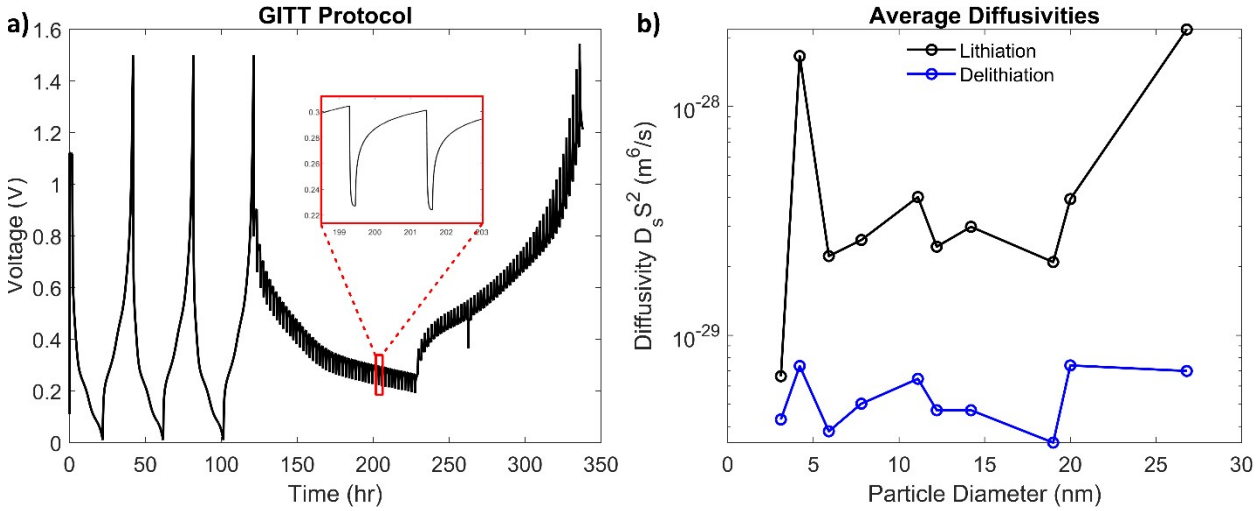

Figure S4: GITT results. a) Example GITT voltage profile, with inset showing current pulses. b) Diffusivity values (reported as D_sS^2), averaged across SOC for each particle size.

To understand if smaller particles still cycle better in higher-carbon content electrodes, electrodes with silicon particle sizes ranging from 3 to 150 nm in diameter were made with 20 wt% silicon, 50 wt% Timcal C45, and 30 wt% polyacrylic acid (PAA). The areal loadings were 0.5 – 0.8 mAh/cm^2. Cycle performances were tested in half cells at a C/3 rate. Figure S5 shows that these higher-carbon content electrodes follow the same trend as the mostly silicon electrodes, where smaller particles have better cyclability. This indicates that smaller particles will still have better cycle lives even in a different electrode architecture (with higher carbon content), and that the extremely dense structure of the Si@PEO electrodes is not what is controlling the improved cycle performance of the smaller particle sizes.

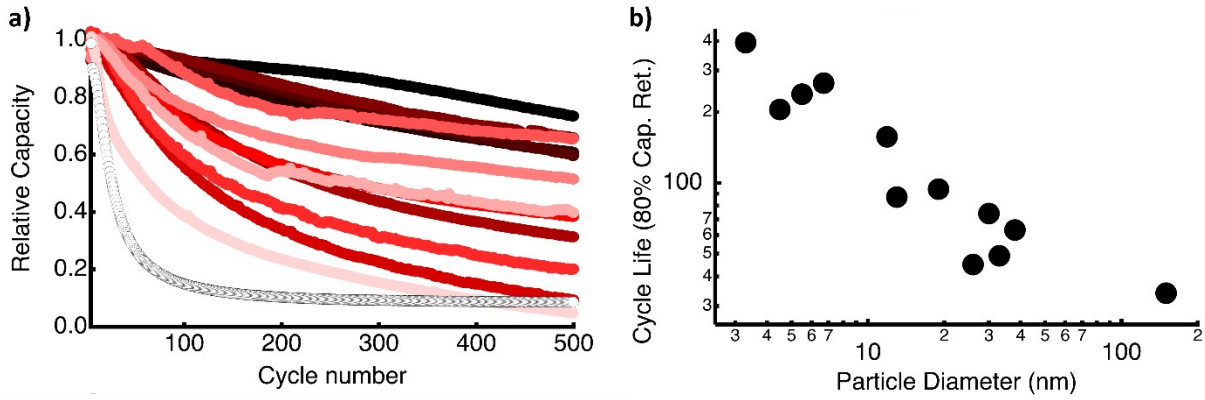

Figure S5: Half cell cycling results from higher carbon-content electrodes. a) Relative capacities of different particles (smaller particles are shown in the darker traces). b) Cycle life (or number of cycles to reach 80% relative capacity) as a function of particle diameter.

Extended Full Cell Electrochemical Results:

The electrochemical protocols for full cell testing against a lithium iron phosphate (LFP) cathode are plotted in Figure S6. Full cells are formed with two full C/10 cycles, followed by a 48-hour voltage hold at 3.4 V to ensure full lithiation of the silicon, followed by ten C/3 cycles. Cycle and calendar life performance, following formation, was tested at 30 and 45 °C, respectively, with intermittent RPT steps to check reversible capacity and impedance. A full reference performance testing step (RPT step) is comprised of three C/10 cycles and a hybrid pulse power characterization (HPPC) test during charge. A HPPC test involved charging the cell at C/10 for one hour, resting for one hour, discharging at 3C for 10 seconds, resting for 40 seconds, charging at 2.25C for 10 seconds, and resting for 60 seconds. This was repeated until the cell was charged; the impedances reported in Figure 2 are calculated from the maximum value from the discharging pulses. In Figure S6, the C/10 cycles are shaded green and the HPPC test is shaded yellow. Cells that were testing cycling performance cycled at a C/3 rate, with an RPT step every 50 cycles. Calendar aging cells had an RPT step every 30 days, with a daily 1C discharge pulse for 30 seconds, followed by a 40 second rest, and then a charge back up to 3.4 V at 0.75C, and a constant voltage hold at 3.4V for 300 seconds. Additional cells continuously repeated the RPTs, without any cycling or calendar aging between, to account for capacity fade due to the RPT step.

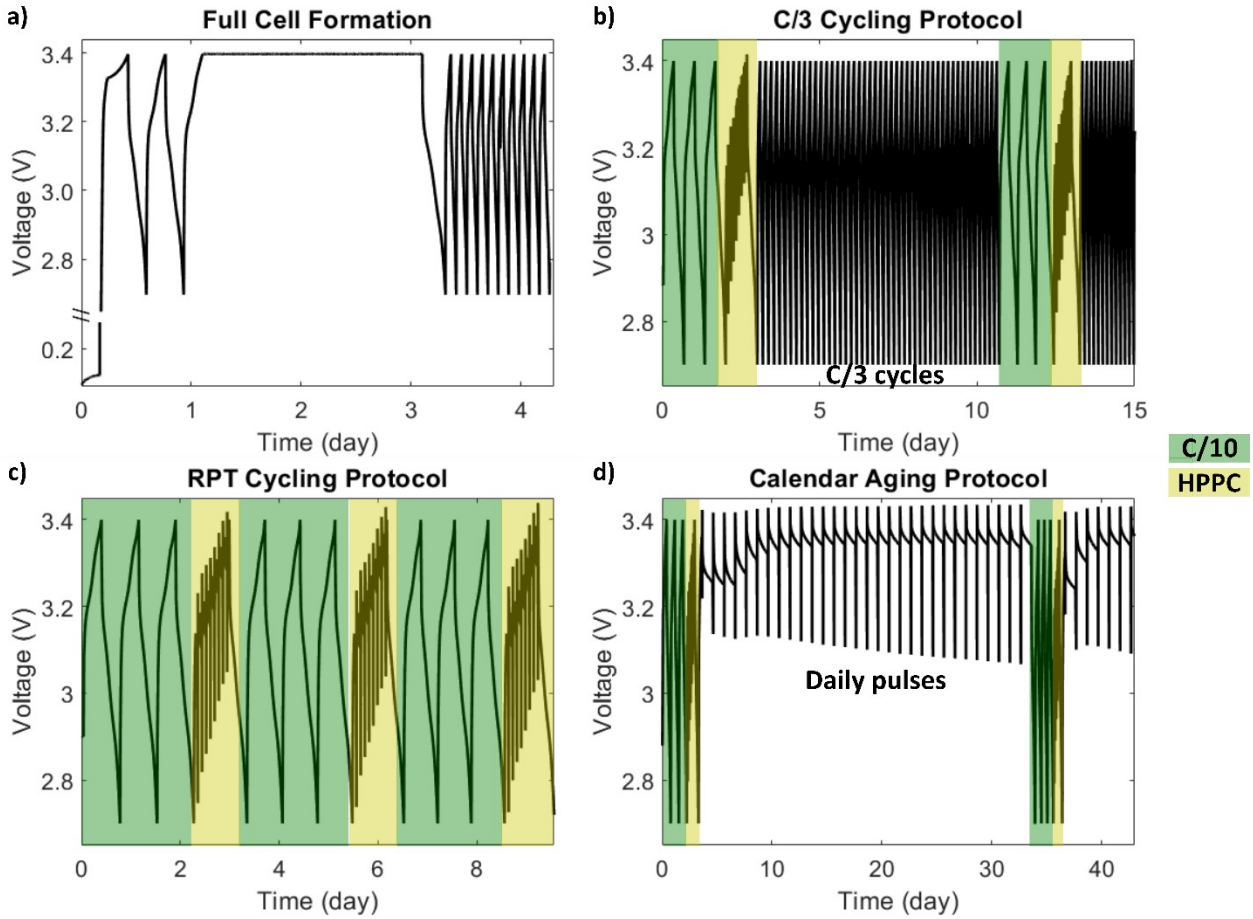

Figure S6: Electrochemical protocols for a) full cell formation, b) C/3 cycling, c) RPT cycling, and d) calendar aging.

The first cycle coulombic efficiencies (CE) during formation for both half and full cells is shown in Figure S7a. Half cells have better CEs mostly due to different voltage windows; half cells were cycled in the full voltage range (0.01 – 1.5 V) but full cells were cycled in a smaller voltage window (2.7 – 3.4 V). Smaller particles require more lithium in the first lithiation step to amorphized the crystalline silicon, and therefore have lower first cycle CEs. These large first cycle losses are why the N/P ratios were initially set to 0.40 to 0.85, as these cells were not prelithiated before cycle or calendar aging, and an oversized cathode was required to provide enough lithium for formation. We do not believe the N/P ratio variations between electrodes had a significant impact on results, as the N/P ratios were not significantly correlated with any other metrics in Figure 5.

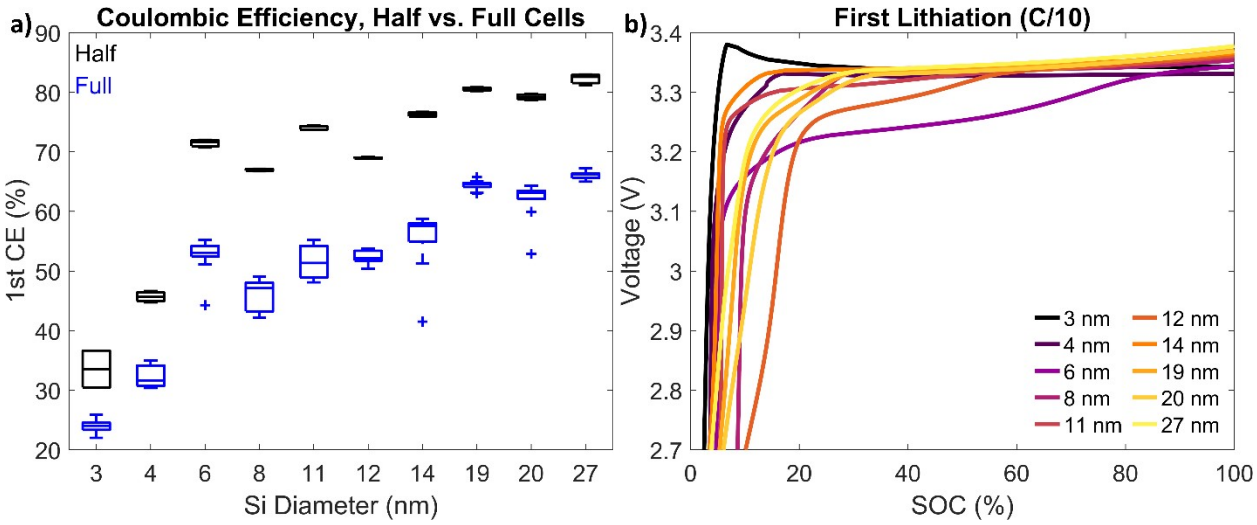

Figure S7: First cycle lithiation and coulombic efficiencies. a) First cycle coulombic efficiencies (CE) for half and full cells for each electrode. b) First lithiation voltage curve (at a C/10 rate) for full cells versus LFP.

Table S3: Estimation of the N/P ratio after formation cycle losses.

Particle diameter (nm)	**Average formation cycle cumulative charge losses (mAh/cm^2)**	**N/P ratio after initial cycles**	**Average number of C/3 cycles to reach N/P of 1**
3	1.1	0.57	194
4	1.0	0.72	99
6	0.71	0.75	89
8	0.78	0.70	90
11	0.73	0.80	59
12	0.58	0.47	241
14	0.61	0.63	79
19	0.55	0.67	56
20	0.63	0.74	52
27	0.59	0.78	32

The average (over 2-3 replicate cells) initial cumulative charge losses were calculated as the difference in charge and discharge capacities for the formation cycles and shown in Table S3. We assume that these initial losses are lithium that is removed from the usable capacity of the 1.7 mAh/cm^2 LFP cathode, and therefore calculate the N/P ratio (after initial cycles) as $\frac{Q_{nom}}{1.7 - Q_{loss}}$ where Q_{nom} is the nominal capacity of the cell (defined as the average between the second and third discharge C/10 cycles of the first RPT test after formation), and Q_{loss} is the cumulative charge losses from the formation cycles. After formation, the cells are still anode limited. However, the choice of LFP should limit aging problems due to the cathode. Also, we can see from dQ/dV plots (see Figure 1 and Figure S11) that there are no lithium plating issues. While optimal performance is known to occur in cathode-limited cells, we can conclude that our oversized cathodes do not

affect the trends we see in cyclability or the lack of trend we see in calendar aging (as seen from the correlation plot in Figure 5). We also calculate the number of cycles that the C/3 cycling cells needed to reach an N/P ratio of 1 (i.e. the cumulative losses from formation plus cumulative losses from cycling equals 1.7 - Q_{nom}). After around 80-100 cycles for most electrodes, the cells are actually cathode limited. This is corroborated by the loss of lithium inventory dQ/dV signatures seen in Figure S11, where the higher voltage peak loses capacity first.

Figure S8 is Figure1a, reproduced in a larger format for better visibility. The ending C/10 cycle capacity is labeled with the corresponding particle size. From Figure 1, there appears to be some correlation between applied current densities and cycle life, as typically larger particles resulted in higher loading electrodes. To see if this affects our results, we ran the C/3 cycling protocol on larger particle-sized electrodes but set the C-rate to be equal to the lowest loading rate (3 nm cells, 0.7 mA for a 1C rate). This was equivalent to around a C/6 cycling rate for the higher loading 6, 20, and 27 nm cells. The results are shown in Figure S9. There is no significant difference in cycling performance between a C/3 and C/6 cycling rate, indicating that the difference cycling performances of different particle sizes is not controlled by the applied current density.

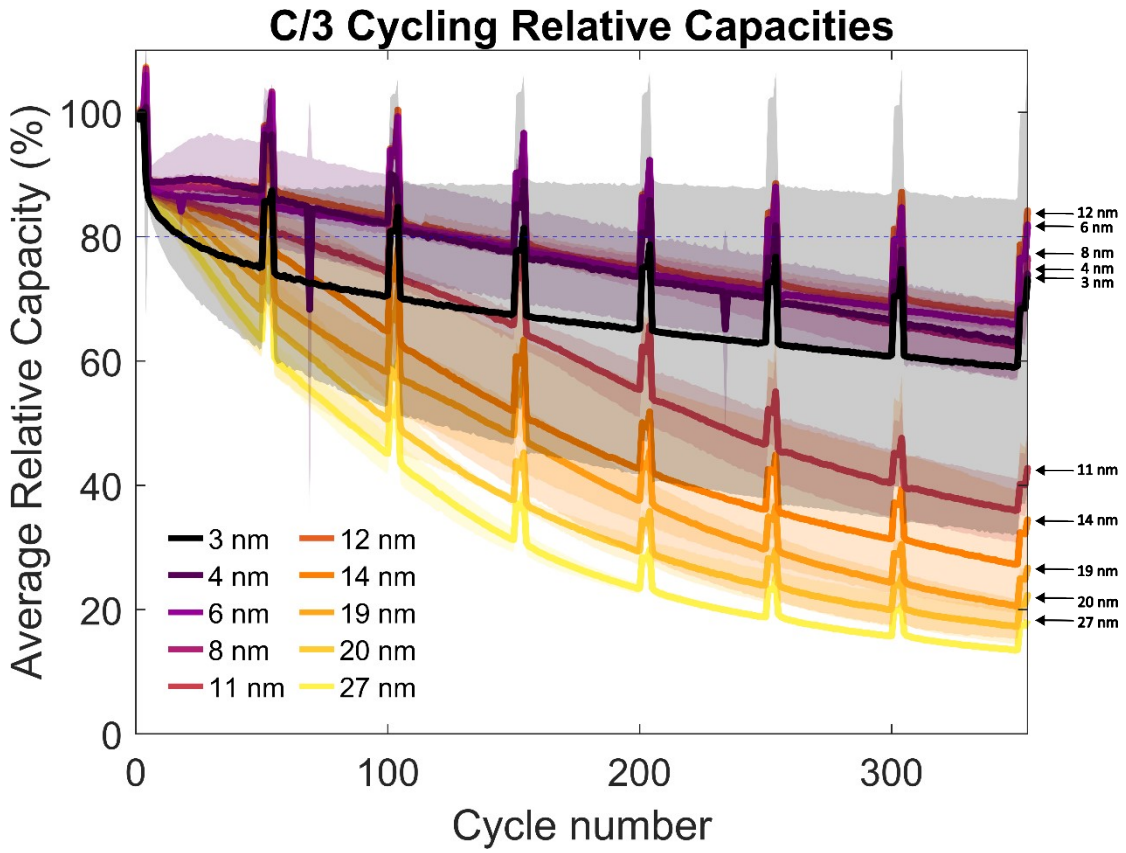

Figure S8: A larger format of Figure 1a, with labels indicating where the last C/10 RPT capacity at 350 cycles is for each particle size.

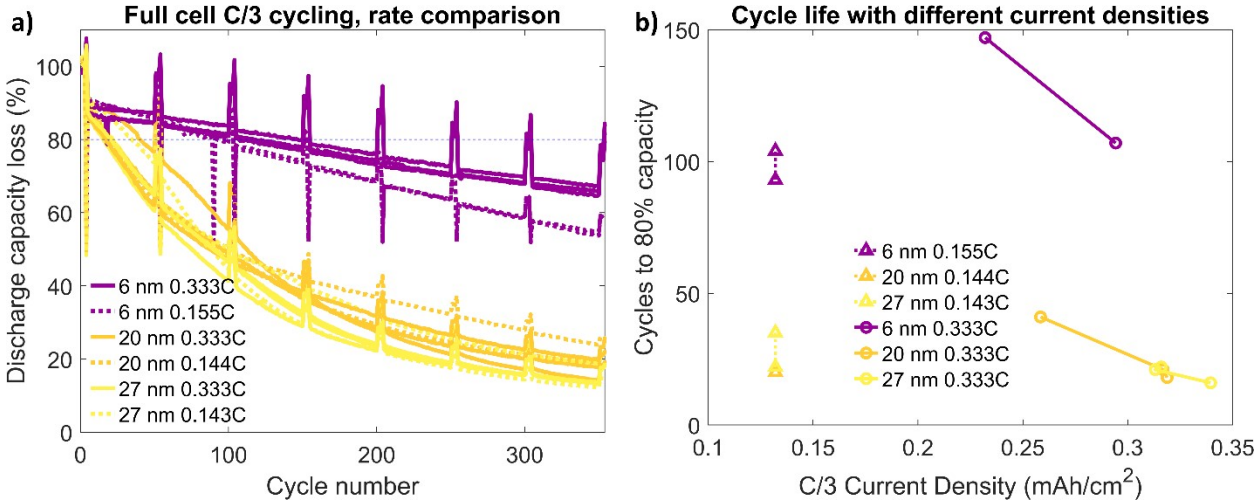

Figure S9: Comparison of C/3 cycling cells for some electrodes at different applied current densities. b) Cycle lifetimes versus applied current density.

The results of the calendar aging and RPT cycling cells over time are shown in Figure S10. Also shown is the calculated contribution of calendar aging to capacity fade and area specific impedance (ASI) rise, which is calculated by removing the amount of capacity loss (or impedance rise) measured from the RPT cycling cells from the calendar aging cells for each RPT (equation 4, where superscripts CalContrib, CalAging, and RPTCycling refer to the calendar aging only contribution, the calendar aging cells, and the RPT cycling cells, respectively. Subscripts RPTX and RPT1 correspond to the ASI results for a given RPT (X) and for the first cycle RPT result (1)). This is an estimate of how the cells would age without any cycling. It is worth noting that the 3 and 4 nm electrode RPT cycling cells experience a decrease in ASI, likely due to issues with wetting or fully utilizing the electrode (as discussed in the half cell results Figure S2, which show that it requires many cycles (and an infinite lithium inventory) to fully utilize the 3 and 4 nm silicon electrodes, likely due to issues with lithium percolation in these dense electrodes). The formation for full cells (a total of 13 cycles and a 48 hour hold at the top of charge) likely mitigates the significant wetting issue seen in the half cells (which only had three C/20 cycles as a formation). However, the 3 and 4 nm particles require significant lithium inventory to fully wet, and this might be why the wetting issue is only visible for them in full cells. The ASI rise for cells with particles sizes greater than 6 nm are very similar, and there is not a clear trend with the speed of capacity fade and particle size.

$$\Delta ASI_{RPTX}^{CalContrib} = \left(ASI_{RPTX}^{CalAging} - ASI_{RPT1}^{CalAging}\right) - \left(ASI_{RPTX}^{RPTCycling} - ASI_{RPT1}^{RPTCycling}\right) \quad (4)$$

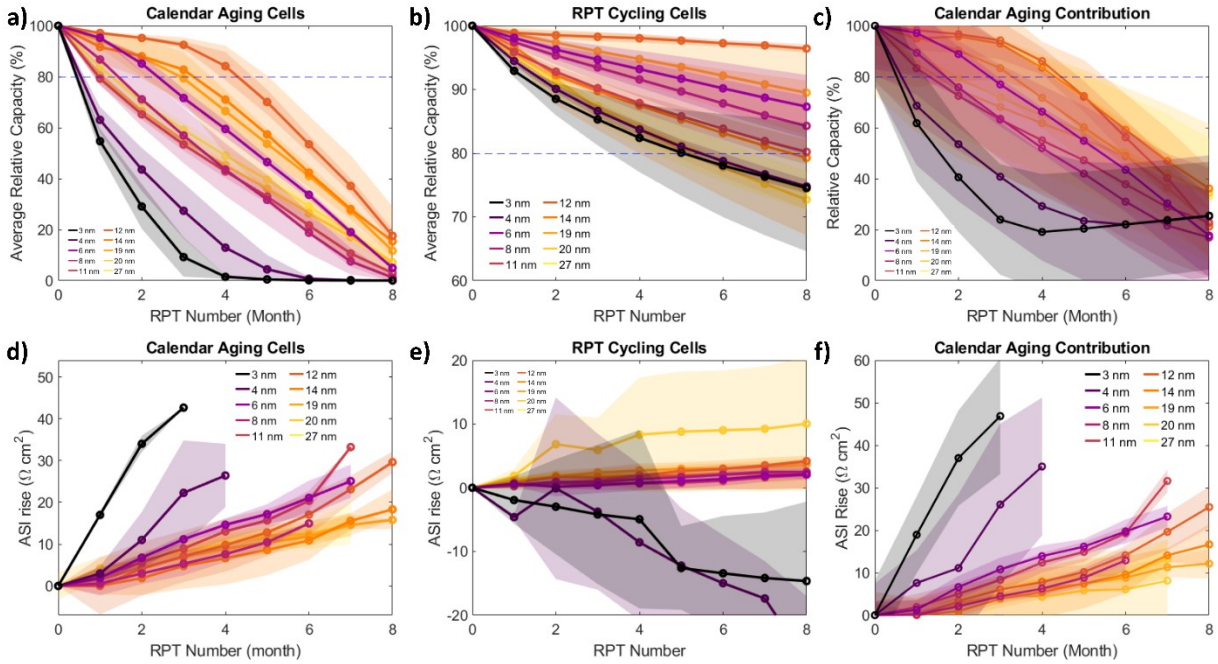

Figure S10: Calendar aging results for calendar and RPT cycling cells. (a-c) Average relative capacities for the calendar aging cells, RPT cycling cells, and the calculated calendar aging contribution, respectively. (d-f) Average ASI rise for the calendar aging cells, RPT cycling cells, and the calculated calendar aging contribution, respectively.

The differential capacities (dQ/dV) for each type of full cell (C/3 cycling, RPT cycling, and calendar aging) are shown in Figure S11. The third C/10 cycle for each RPT step is shown (every 50 cycles for C/3 cells, every 4 cycles for RPT cycling cells, and every 30 days for calendar aging cells). The dQ/dV are normalized to the maximum value for the first RPT. For all electrodes, the higher voltage dQ/dV peaks lose capacity first, indicating a loss of lithium inventory (LLI) as opposed to a loss of active material (LAM), as the main driver of capacity fade. There is no sign of a lithium plating signature in these dQ/dV plots [16].

The voltage hysteresis of every third C/10 cycle for each RPT step was calculated as the difference between lithiation and delithiation voltages at the same state-of-charge (SOC). The average voltage hysteresis, from the middle third of the voltage window, is shown in Figure S12, plotted against capacity fade. With the exception of the 3 and 4 nm electrodes, the hysteresis is similar across electrodes.

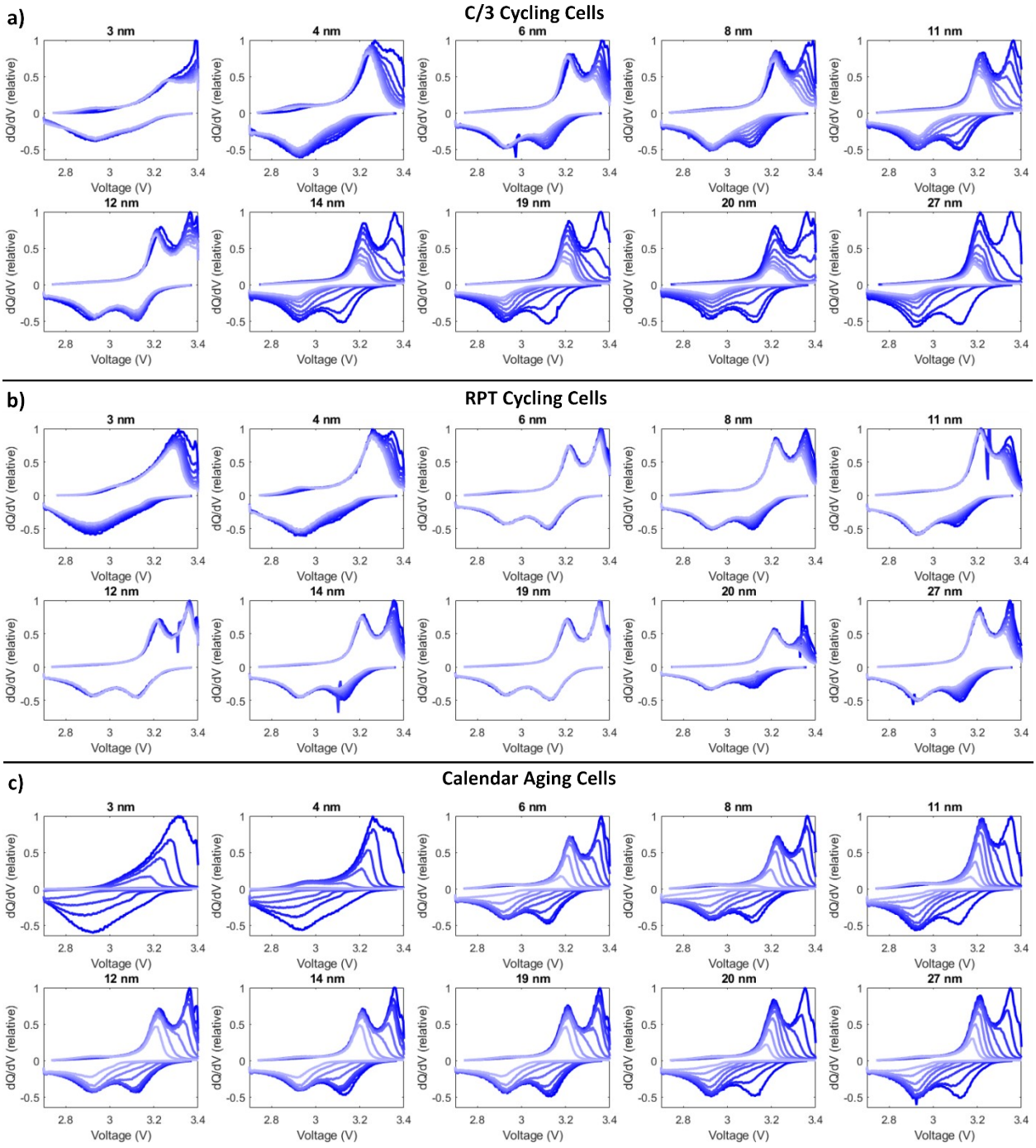

Figure S11: Differential capacity curves for the third C/10 cycle every RPT for a) C/3 cycling cells. b) RPT cycling cells. c) Calendar aging cells. Higher cycle numbers are plotted in lighter shades of blue.

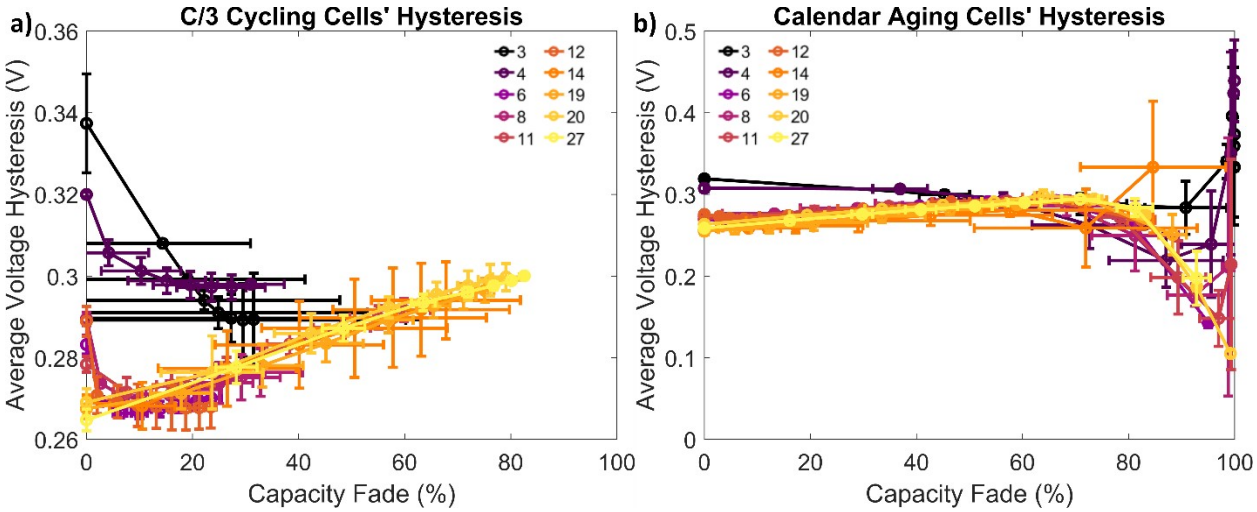

Figure S12: Average voltage hysteresis versus capacity fade for the third C/10 cycle every RPT for a) C/3 cycling cells. b) Calendar aging cells.

SEI Characterization:

After 360-400 cycles, C/3 cycling cells were fully discharged at a C/10 rate, and then disassembled to harvest the electrode. The anode was washed for ~10 seconds with dimethyl carbonate (DMC) to remove excess $LiPF_6$ but not significantly affect the solid-electrolyte interface (SEI). Figure S13 shows pictures of the silicon and copper sides from disassembled cells. Some electrodes have wrinkles or dimples of the copper foil, which is consistent with other silicon anode results, albeit in higher-loading and larger-format cells and is caused by the large volume expansion of silicon [17]. The dense electrode structure might magnify this problem by transmitting large stresses to the copper. To enable higher-loading and larger cells, this problem will need to be mitigated by some form of stress relief in the cell.

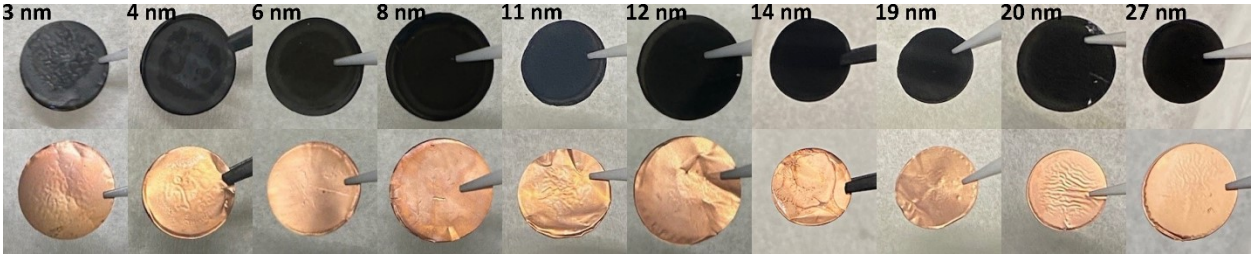

Figure S13: Images of cycled electrodes after rinsing, silicon and copper sides.

X-ray photoelectron spectroscopy (XPS) was performed on these harvested cycled electrodes (Figure S14). There does not appear to be a clear difference between SEI components of different particle sizes, except for the 3 and 4 nm electrodes which have higher $LiPF_6$ which might indicate the washing step for these electrodes was not sufficient to remove dried electrolyte salt. To estimate the ratio of inorganic to organic components of the SEI, we compare the ratio of $LiCO_3$ to C-O bonds as a function of particle size in Figure S15. There is no clear trend with particle size, suggesting that the SEI is similar across all electrodes.

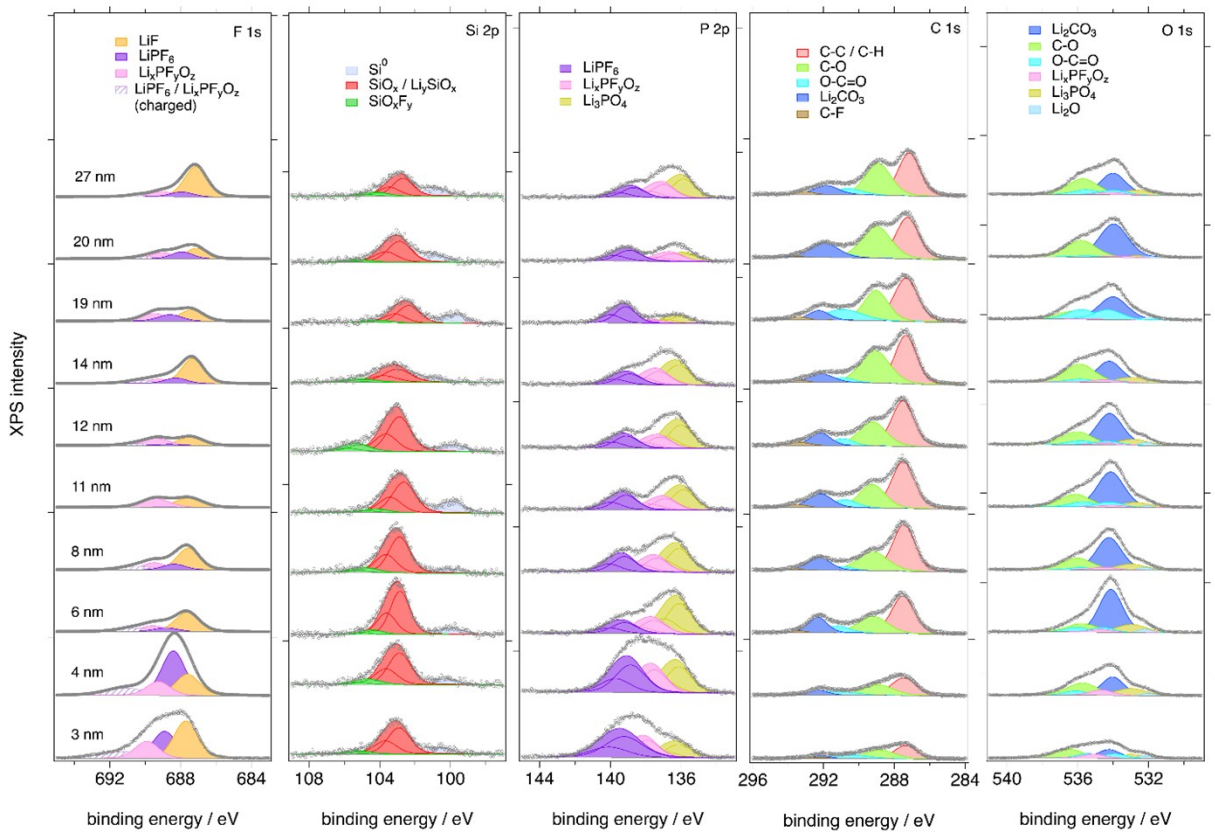

Figure S14: XPS results summary for all ten cycled electrodes.

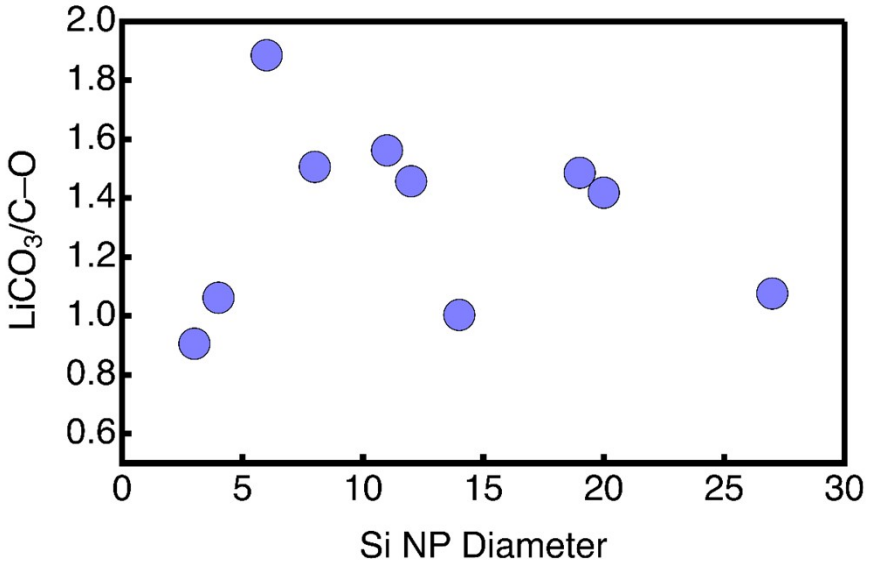

Figure S15: Ratio of organic (C-O) to inorganic (^{LiCO_3}) species in cycled cells' SEI, from XPS results.

Extended Microstructure Characterization:

Using a scanning electron microscope (SEM), ion beam cross-section samples were imaged. Pristine electrode samples were taken from electrode scraps, and cycled samples were taken from one of the full cell C/3 cycling coin cells (a different segment of the cycled electrode was used for the XPS results). Every attempt to limit air exposure was made, but the ion beam and SEM instruments did not have an air-free holder, so the samples did spend a few minutes in air.

The nanoscale porosity for all particle sizes is shown in Figure S16. The pristine electrodes with smaller particles are so dense that it is hard to resolve any nano-porosity that might exist. Some of the porosity might be below the resolution limit of the SEM. Pristine samples with larger particle sizes appear to have slightly higher porosity (or the pore sizes are larger so it is more visible). Note that some of the porosity in the cycled electrodes is from damage from the SEM beam, but even without the beam damage the cycled samples are much more porous, indicating mechanical damage was caused by the volume change during charge cycling. Estimates of porosity were calculated using image segmentation, using the Microstructure Analysis Toolbox (MATBOX) [18, 19].

Cross-section thicknesses were also measured using the SEM and shown in Figure S17. Using these measurements, taken from multiple points along the electrode, the total electrode expansion was calculated (Figure 3). There are huge volumetric changes due to cycling for all electrodes. Part of this might be due to air exposure, but other contributions include mechanical damage due to particle expansion and SEI formation.

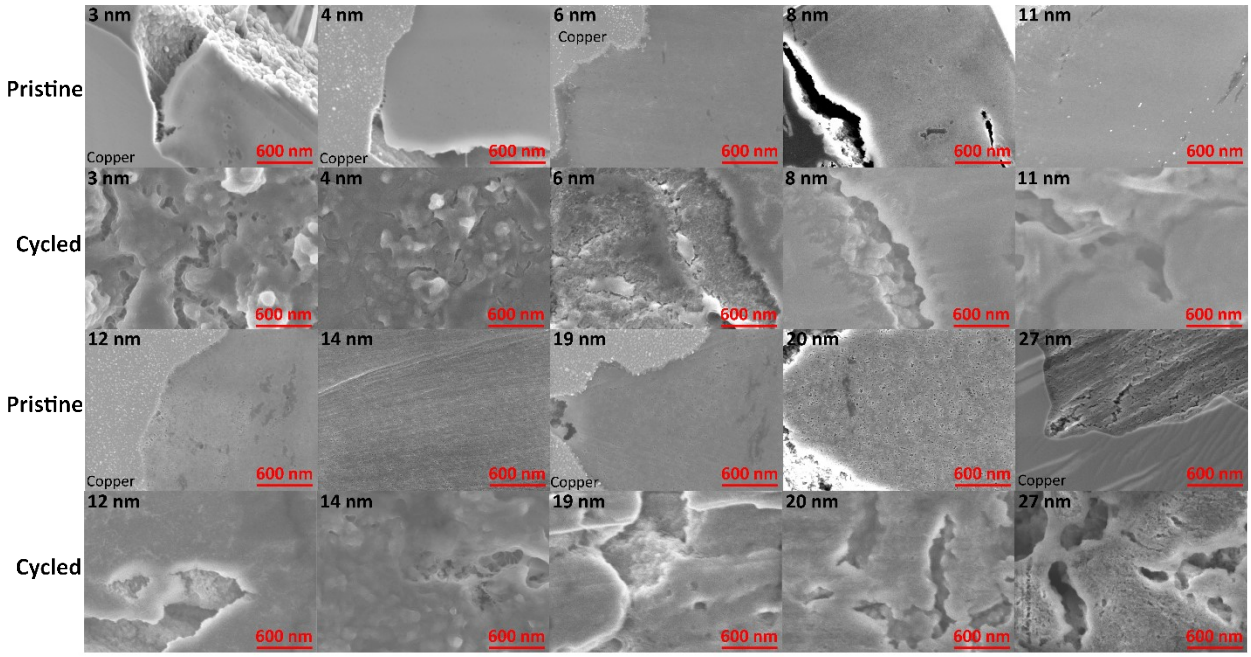

Figure S16: SEM cross-section images of porosity of pristine and cycled electrodes.

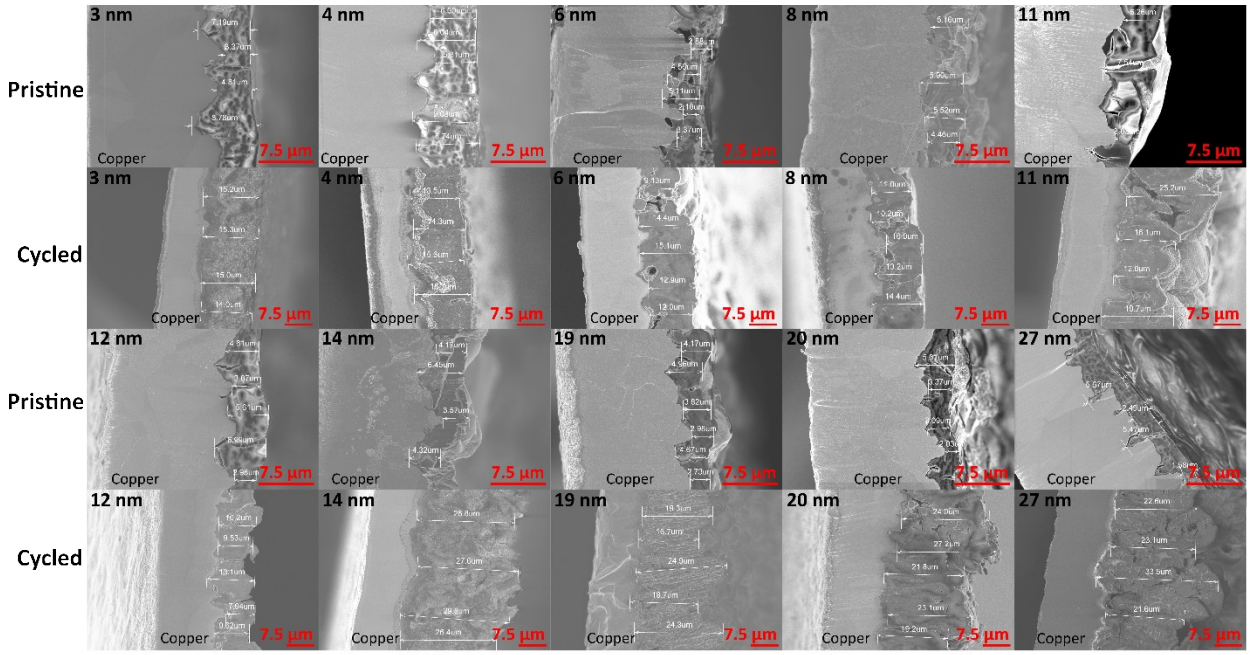

Figure S17: SEM cross-section images of electrode thickness variations of pristine and cycled electrodes.

There is also microscale porosity in the form of cracks in every pristine electrode, shown by SEM images of the top-down view (Figure S18). The morphology of the electrodes, particularly the 3 and 4 nm samples, does vary. Possible reasons include differences in drying conditions; while every attempt to be consistent was made, it is possible the thinner electrodes might have started to dry before they were placed in the oven. Additionally, the solids loading of the slurry varied slightly due to the different amounts of PEO coating (as shown in Table S2), which might have affected microscale electrode morphology. After cycling, the 3 and 4 nm electrodes retain the mud-cracked structure, but the cracks appear to be filled in. Additionally, the electrodes with 6 nm and greater particle sizes appear to have similar morphologies after cycling, but the height of the growths seems to increase with capacity fade (larger particles were harvested from a sample with more capacity loss, see Figure S19).

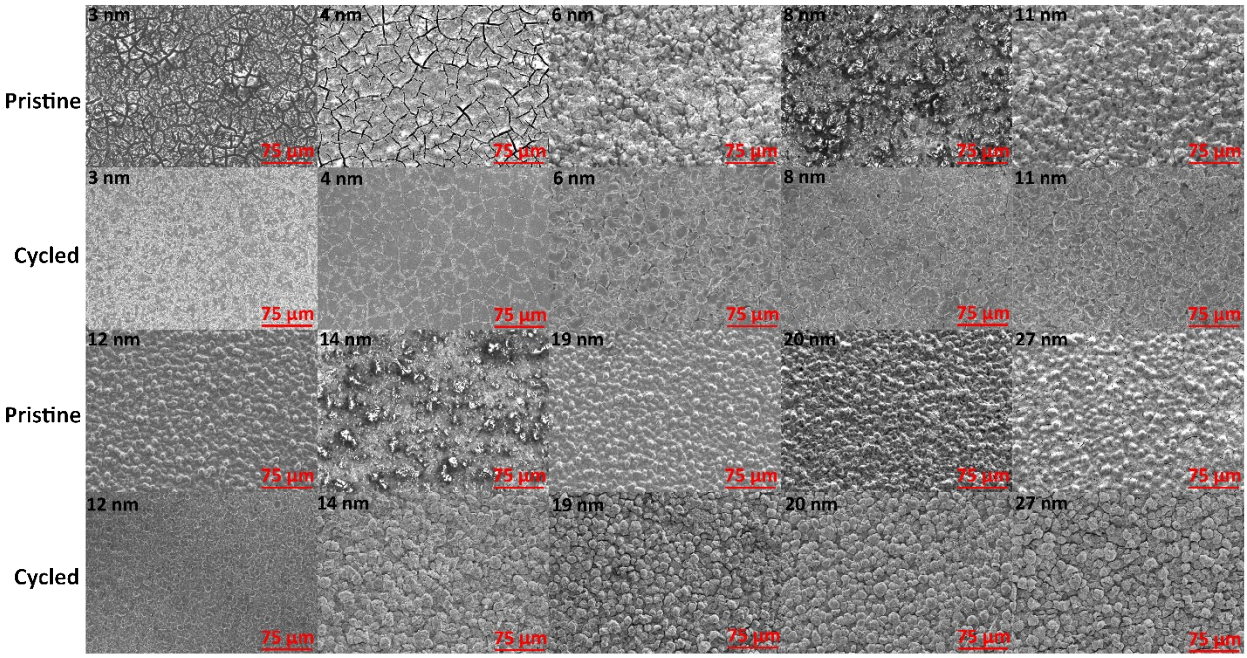

Figure S18: SEM top-down images of pristine and cycled electrodes.

Figure S19 shows the correlations for the cells used for the SEM cross-sections (after cycling). Linear correlations (including all electrodes and excluding the 3 and 4 nm electrodes) between the particle diameter, coin cells' capacity at the end of cycling (~350 cycles), silicon utilization, cycle life, and calculated expansion based on the SEM cross-section measurements from this coin cell and pristine measurements from another area of the electrode. We can see there is a correlation between the ending relative capacity and the electrode expansion after cycling. This makes sense, as larger expansions mean more mechanical damage and SEI formation, which would lead to faster capacity fade.

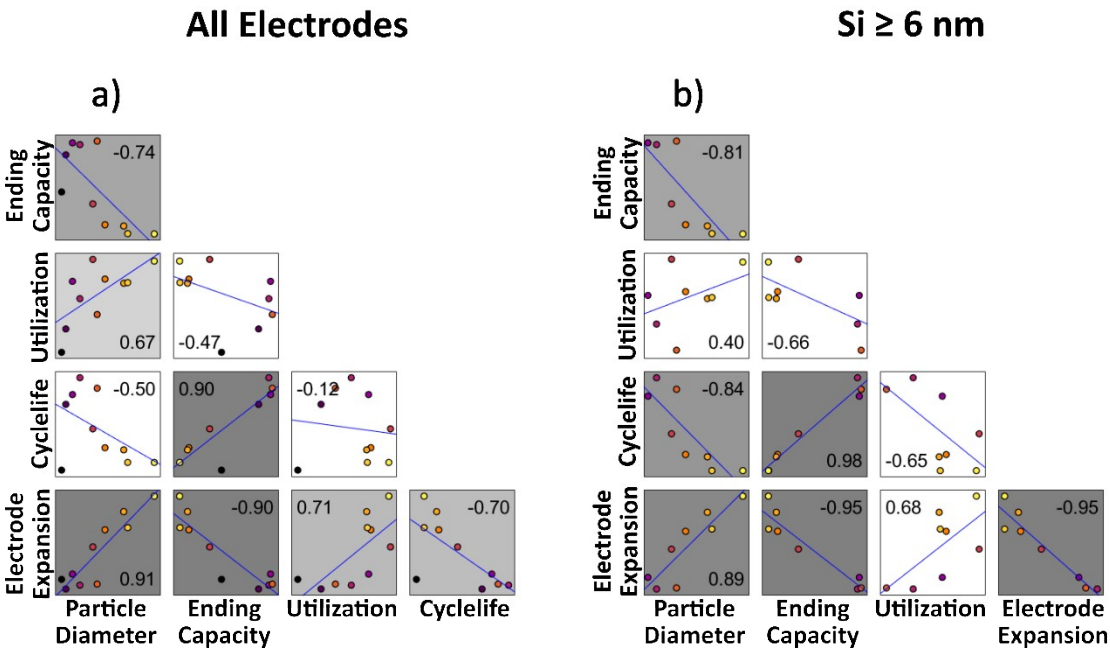

Figure S19: Linear correlations between cross-section coin cells' performance. Shaded boxes indicate significant correlations, based on a p-value of 0.05 (equivalent to a 95% confidence threshold). Points are color-coded for particle size. There are no error bars because this represents only one coin cell result. a) Correlations for all electrodes. b) Correlations excluding 3 and 4 nm electrode outliers.

Brunauer-Emmett-Teller (BET) surface area analysis was performed on representative electrodes (Table S4). Because the sample size requirements of BET were too much for the authors to measure the electrodes used in this study, other, similar, electrodes were characterized. One electrode used 6 nm PECVD Si functionalized with PEO, Tuball carbon nanotubes, and a polyimide binder (with PVDF dispersant that is assumed to not be burned off during annealing), in a 92:1:5:2 Si:SWCNTs:polyimide:PVDF ratio, and was annealed at 420 ℃ for four hours. This electrode is expected to be similar in structure to this paper's 6 nm electrode. Additionally, to see the effect of the carbon morphology, an electrode made with 6 nm PECVD (functionalized with PEO), carbon black (Timcal C45), and polyimide binder, with ratios of 80:10:10 Si:C:polyimide, and annealed at 550 ℃ for four hours. The surface area using MBET is orders of magnitude higher than what is measured with symmetric coin cells (from Figure 4, the 6 nm electrode has around 2 cm^2/cm^2 active area, or around 1.3 m^2/g for an electrode that weighs 1 mg). This is because gas molecules are much smaller than electrolyte molecules and get can into the nano-sized pores in the electrode. It is worth noting that the predicted surface area from the computational model (~1200 cm^2/cm^2 for 6 nm, or 200 m^2/g) is similar to the BET measurements for a SWCNT electrode. So, BET is able to measure the full surface of the electrode, but this full surface is not being used in a coin cell because the electrolyte molecules are too big to fit through the pores.

Table S4: BET surface area analysis.

Sample (carbon)	Silicon Mass (mg)	MBET Surface area (m^2/g)	DFT Surface area (m^2/g)	DFT Pore Volume (cc/g)	DFT Pore Diameter (nm)	MBET Total Surface Area (m^2)
SWCNT	21	430	306	0.335	3.8	9.0
C45	57	70	48	0.054	3.5	4.0

Computational Microstructure Extended Results:

The microstructure of an electrode with 3, 9, 15, and 30 nm Si particle sizes was modeled using the Microstructure Analysis Toolbox (MATBOX) [17, 18]. Electrode microstructures were generated with 1 wt% SWCNT, 10 wt% P84, and 89 wt% Si, at three porosities (20, 30, 40%), with four silicon particle diameters (3, 9 ,15, and 30 nm). More details about the generation algorithms and other results are available in [20]. Figure S20 displays example microstructure images generated with this toolbox. For smaller particles (3, 9, and 15 nm diameters) the carbon nanotubes were generated first, and then the silicon particles filled in gaps between them until the target porosity was reached. Two different geometry assumptions for the SWCNTs were made: isotropy, and transversal anisotropy, where the carbon nanotubes are preferentially oriented transversely to the electrode. For the 30 nm particle, the silicon particles were generated first, followed by the nanotubes, where the resulting nanotube geometry was controlled by the nanoparticles that had previously been generated.

The silicon-to-silicon particle contact area and silicon-to-pore areas for different particle diameters are shown in Figure S21. In general, the model predicts a decrease in connectivity between silicon particles for increasing particle size. Additionally, connectivity increases for lower porosities, which makes sense as a denser structure would have more contact points. The isotropic versus anisotropic assumption for the nanotubes makes little difference in connectivity, except for the smallest particle, which has a similar diameter as the diameter of the nanotube.

The silicon-to-pore area is what we would expect to be similar to the electrochemically-active surface area (ECSA), as this value reports the total area of silicon exposed to a pore or void. However, due to the low porosities of these Si NP electrodes, the pores are too small for electrolyte to actually infiltrate into the pores, so the actual ECSA is much lower than the computational model predicts. Regardless, the model predicts that the theoretical ECSA decreases for larger particles, which makes sense as the surface-to-volume ratio decreases as well. Lower porosity electrodes would have less exposed Si surface area, also as expected. The nanotube geometry does not make much of a difference, except for the smallest particle, similar to the silicon-silicon connectivity results.

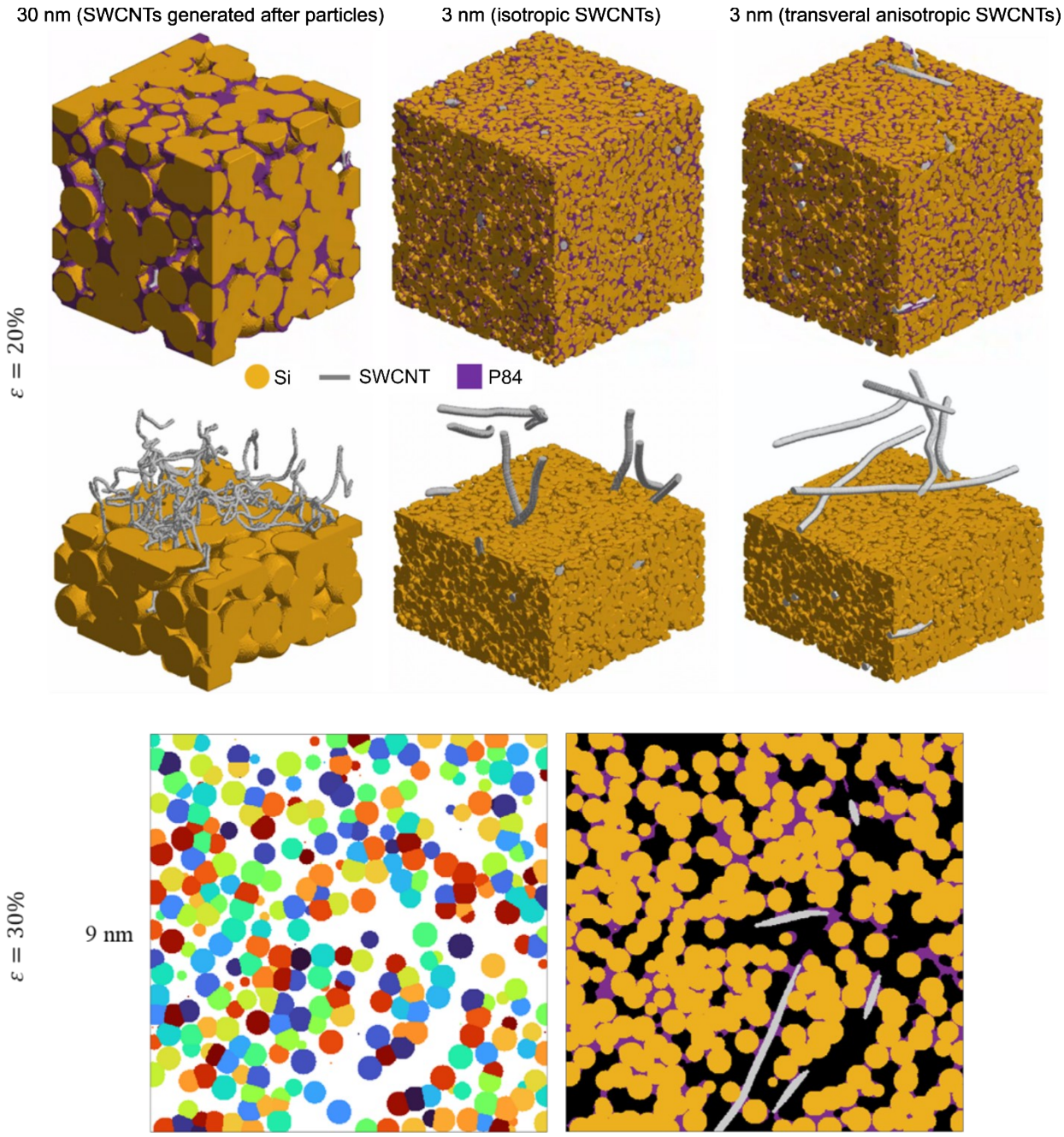

Figure S20: Example of numerically generated silicon anodes. (top and middle row) 3D visualizations of 20% porous electrodes with 30 and 3 nm silicon particle diameter, with SWCNT orientation being either, from left to right, controlled by the large Si particles, isotropic, or transversal anisotropic. (bottom row) Cross-section view of a 30% porous electrode with 9 nm silicon particle diameter, with (left) particle labels, used to deduce interface area between silicon particles in contact and (right) phase labels, used to deduce interface area between silicon particles and the pore domain. Note that pores within particle agglomerates are systematically filled with the binder phase, letting only pore-Si interface at the surface of the agglomerates.

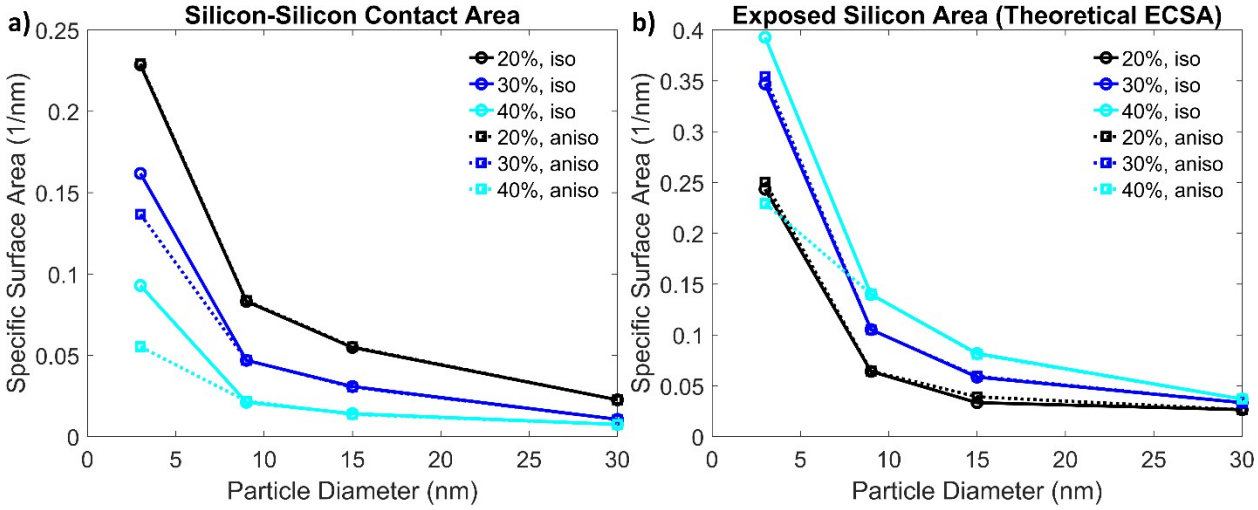

Figure S21: a) Si-Si connectivity specific surface area. b) Si-pore (theoretical ECSA) specific surface area.

Correlation Calculations:

The Pearson correlation coefficient (R) was calculated using:

$$R = \frac{\frac{cov(A,B)}{\sigma_A \sigma_B}}{\left(1+\left(\frac{\sigma_{A,e}}{\sigma_A}\right)^2\right)\left(1+\left(\frac{\sigma_{B,e}}{\sigma_B}\right)^2\right)} \quad (5)$$

Where A and B are the variables being correlated, σ_A and σ_B are their respective standard deviations [21]. It is typical to assign $\sigma_{A,e}$ and $\sigma_{B,e}$ as the standard deviation of the errors, but that requires knowledge of the expected values, which we don't have from triplicate coin cell results. Therefore, $\sigma_{A,e}$ and $\sigma_{B,e}$ are the standard deviations of the standard deviations, and $cov(A,B)$ is the covariance between A and B.

The standard deviations σ for aging and impedance rise due only to calendar aging was calculated using propagation of errors, where x and y are the measured values that each have standard deviations σ_x and σ_y, and covariance σ_{xy} [22]:

$$\sigma(x-y) = \sqrt{\sigma_x^2 + \sigma_y^2 - 2\sigma_{xy}} \quad (6)$$

$$\sigma\left(\frac{x}{y}\right) = \left|\frac{x}{y}\right| \sqrt{\frac{\sigma_x^2}{x^2} + \frac{\sigma_y^2}{y^2} - \frac{2\sigma_{xy}}{xy}} \quad (7)$$

From the Pearson correlation coefficient, we can calculate the p-value, or probability that the variables are correlated. Any correlation with a p-value lower than 0.05 (corresponding to a confidence of 95%) was determined to be significant. The p-value can be calculated from a t-test where the null hypothesis is there is no correlation, and there are $n-2$ degrees of freedom (n is the number of observations). The t-statistic t can be calculated from the Pearson coefficient R using:

$$t = \frac{\sqrt{n-2}\,R}{\sqrt{1-R^2}} \tag{8}$$

To convert the t-statistic to a p-value (p), we use a look-up table for the t-statistic with $n-2$ degrees of freedom (in Matlab, the tcdf function):

$$p = 2 * min[tcdf(|t|,n-2), 1-tcdf(|t|,n-2)] \tag{9}$$

Where p is twice the minimum of $tcdf(|t|,n-2)$ or $1-tcdf(|t|,n-2)$.

For the linear fits in the correlation plots, when both variables had no error associated with them (like diameter or S/V), a typical least-squares regression was used. When one of the variables had measurement errors, a least-squares regression with weights was used, where the weights were calculated as:

$$w_i = \frac{\sigma_i^{-2}}{\sum_{i=1}^{n} \sigma_i^{-2}} \tag{10}$$

Where w_i is the weight of each point and σ_i is the standard deviation of that point. w_i was set to 1 if σ_i was 0. If both variables had error values, then a Deming regression was used to calculate the best linear fit, using [23]:

$$m = \frac{(\lambda\sigma_B^2 - \sigma_A^2) + \sqrt{(\sigma_A^2 - \lambda\sigma_B^2)^2 + 4\lambda cov(A,B)^2}}{2\lambda cov(A,B)} \tag{11}$$

$$b = \bar{B} - m\bar{A} \tag{12}$$

Where m is the slope of the best fit line and b is the intercept. λ is the ratio of variances of the errors of A and B, or $\sigma_{B,e}^2/\sigma_{A,e}^2$. $cov(A,B)$ is the covariance of A and B, and $\bar{A}$, $\bar{B}$ are the mean values of A and B. Table S5 lists each correlation variable and its corresponding units and measurement information.

Figure S22 shows the correlations between the metrics listed in Table S5, including all electrodes. Different correlations become significant when we include all electrodes (as compared to electrodes with 6 nm particles or greater, in Figure 5). Particle diameter, coulombic efficiency, and cycle life are no longer correlated to each other, as the 3 and 4 nm performed much worse than the other electrodes in calendar aging, are biasing these correlations. New metrics become correlated in Figure S22, including several significant correlations with calendar aging and impedance rise, all biased by the 3 and 4 nm electrode performances. Areal and specific capacity are correlated to particle diameter, as utilization drops precipitously in particles below 6 nm (as seen in Figure 1c). This is another indication that the smallest particle sizes have significant trade-offs.

Table S5: List of correlation variables, descriptions, units, and where the measurements were calculated from.

Variable Description	**Units**	**Measurements are from**	**Number of measurements**
Particle diameter	nm	XRD	1
Electrochemically active surface area	cm^2/cm^2	Blocking electrolyte symmetric cell	1
Si-to-Si particle contact area	$1/nm$	Microstructure model, values interpolated	Interpolated
Electrode expansion	%	SEM cross-section images	1
Anode capacity to cathode capacity ratio	-	Full cells	> 6
Areal capacity in full cells	mAh/cm^2	Full cells	> 6
Specific capacity	Ah/g	Full cells	> 6
C/3 cycle lifetime to 80% capacity	Cycles	C/3 cycling cells	> 2
Coulombic efficiency, first 50 C/3 cycles	%	C/3 cycling cells	> 2
Relative capacity after 3 months (calendar aging)	%	Calendar aging contribution, from calendar aging and RPT cycling cells	> 2
Impedance rise after 3 months (ASI)	$\Omega\, cm^2$	Calendar aging contribution, from calendar aging and RPT cycling cells	> 2

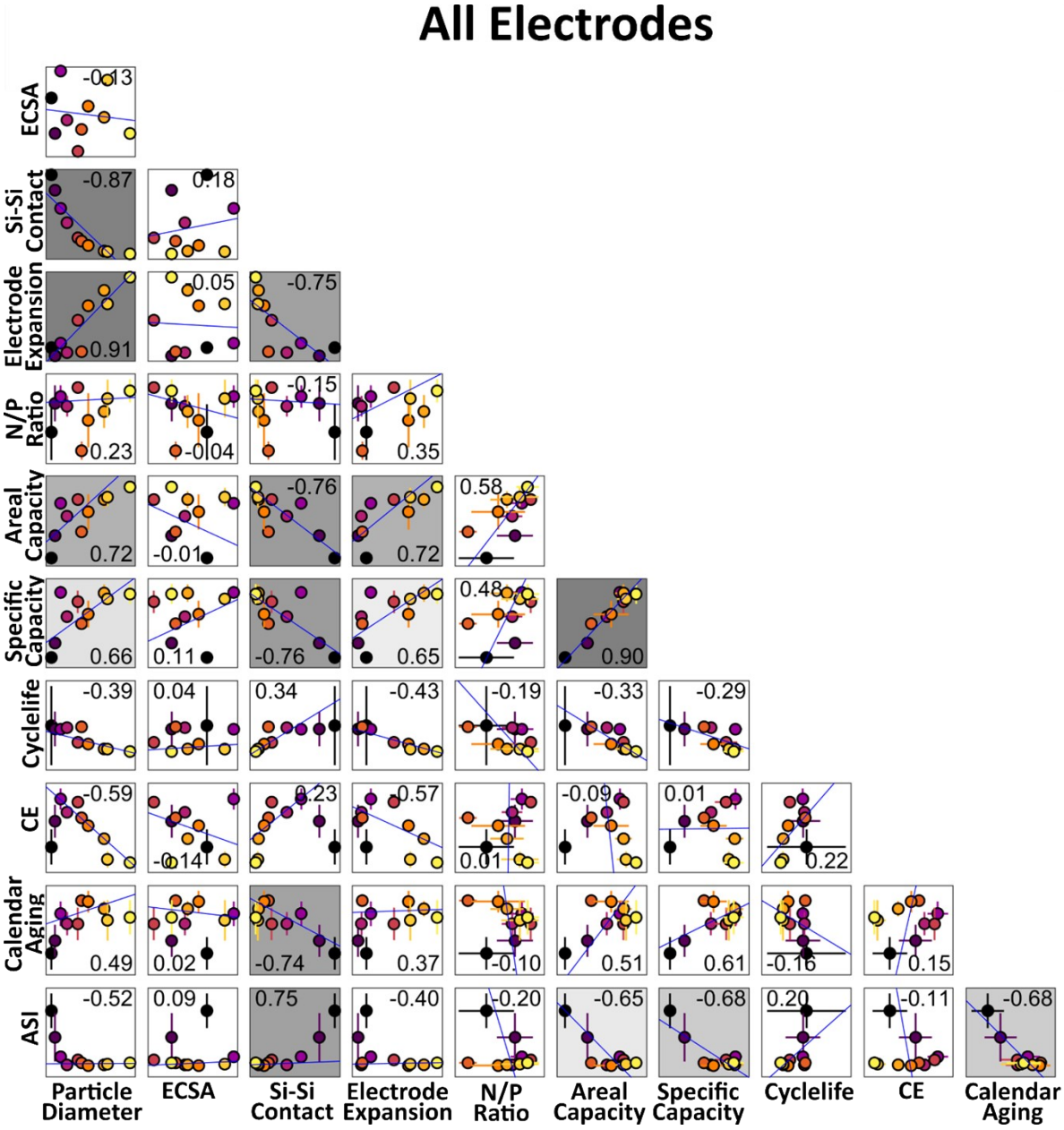

Figure S22: Correlations including 3 and 4 nm outlier electrodes. Correlations here correspond to the ones shown in Figure 5, that do not include the 3 and 4 nm electrode results.

References:

[1] Mangolini L, Thimsen E, Uwe Kortshagen. High-Yield Plasma Synthesis of Luminescent Silicon Nanocrystals. 2005 Mar 5;5(4):655–9.

[2] Wheeler LM, Anderson NC, Palomaki PKB, Blackburn JL, Johnson JC, Neale NR. Silyl Radical Abstraction in the Functionalization of Plasma-Synthesized Silicon Nanocrystals. Chemistry of Materials. 2015 Oct 1;27(19):6869–78.

[3] Carroll GM, Schulze MC, Martin TR, Pach GF, Coyle JE, Teeter G, et al. SiO_2 Is Wasted Space in Single-Nanometer-Scale Silicon Nanoparticle-Based Composite Anodes for Li-Ion Electrochemical Energy Storage. ACS Applied Energy Materials. 2020 Nov 10;3(11):10993–1001.

[4] Schulze MC, Carroll GM, Martin TR, Sanchez-Rivera K, Urias F, Neale NR. Hydrophobic versus Hydrophilic Interfacial Coatings on Silicon Nanoparticles Teach Us How to Design the Solid Electrolyte Interphase in Silicon-Based Li-Ion Battery Anodes. ACS Applied Energy Materials. 2021 Feb 8;4(2):1628–36.

[5] Barai A, Widanage WD, Marco J, McGordon A, Jennings P. A study of the open circuit voltage characterization technique and hysteresis assessment of lithium-ion cells. Journal of Power Sources. 2015 Nov;295:99–107.

[6] Dreyer W, Jamnik J, Guhlke C, Huth R, Moškon J, Gaberšček M. The thermodynamic origin of hysteresis in insertion batteries. Nature Materials. 2010 Apr 11;9(5):448–53.

[7] Jahn L, Mößle P, Röder F, Danzer MA. A physically motivated voltage hysteresis model for lithium-ion batteries using a probability distributed equivalent circuit. Nature Communications Engineering. 2024 May 30;3(1).

[8] Gallagher KG, Dees DW, Jansen AN, Abraham DP, Kang SH. A Volume Averaged Approach to the Numerical Modeling of Phase-Transition Intercalation Electrodes Presented for Li_xC_6. Journal of the Electrochemical Society. 2012 Jan 1;159(12):A2029–37.

[9] Gu M, Wang Z, Connell JG, Perea DE, Lauhon LJ, Gao F, et al. Electronic Origin for the Phase Transition from Amorphous LixSi to Crystalline Li15Si4. ACS Nano. 2013 Jun 28;7(7):6303–9.

[10] Lu B, Song Y, Zhang Q, Pan J, Cheng YT, Zhang J. Voltage hysteresis of lithium ion batteries caused by mechanical stress. Physical Chemistry Chemical Physics. 2016;18(6):4721–7.

[11] Bucci G, Swamy T, Bishop S, Sheldon BW, Chiang YM, Carter WC. The Effect of Stress on Battery-Electrode Capacity. Journal of The Electrochemical Society. 2017;164(4):A645–54.

[12] Verma A, Singh A, Colclasure A. On the Impact of Mechanics on Electrochemistry of Lithium-Ion Battery Anodes. JOM. 2023 Nov 20;76(3):1171–9.

[13] Verma A, Mukherjee PP. Mechanistic Analysis of Mechano-Electrochemical Interaction in Silicon Electrodes with Surface Film. Journal of The Electrochemical Society. 2017 Jan 1;164(14):A3570–81.

[14] Verma A, Smith K, Shriram Santhanagopalan, Abraham D, Koffi Pierre Yao, Mukherjee PP. Galvanostatic Intermittent Titration and Performance Based Analysis of $LiNi_{0.5}Co_{0.2}Mn_{0.3}O_2$Cathode. Journal of The Electrochemical Society. 2017 Jan 1;164(13):A3380–92.

[15] Weppner W, Huggins RA. Determination of the Kinetic Parameters of Mixed-Conducting Electrodes and Application to the System Li3Sb. Journal of The Electrochemical Society. 1977 Oct 1;124(10):1569–78.

[16] Konz ZM, McShane EJ, McCloskey BD. Detecting the Onset of Lithium Plating and Monitoring Fast Charging Performance with Voltage Relaxation. ACS Energy Letters. 2020 May 1;5(6):1750–7.
[17] Rodrigues MTF, Rajendran S, Trask SE, Dunlop AR, Singh A, Allen JM, et al. Cell-Format-Dependent Mechanical Damage in Silicon Anodes. ACS Applied Energy Materials. 2023 Sep 6;6(18):9243–8.
[18] Usseglio-Viretta FLE, Patel P, Bernhardt E, Mistry A, Mukherjee PP, Allen J, et al. MATBOX: An Open-source Microstructure Analysis Toolbox for microstructure generation, segmentation, characterization, visualization, correlation, and meshing. SoftwareX. 2021 Dec 29;17:100915.
[19] Cooper SJ, Bertei A, Shearing PR, Kilner JA, Brandon NP. TauFactor: An open-source application for calculating tortuosity factors from tomographic data. SoftwareX. 2016;5:203–10.
[20] Usseglio-Viretta FLE, Preimesberger JI, Coyle JE, Huey Z, Jiang CS, Kim JH, Neale NR, Carroll GM and Colclasure AM, [In progress].
[21] Francis DP, Andrew J.S. Coats, Gibson DG. How high can a correlation coefficient be? Effects of limited reproducibility of common cardiological measures. 1999 May 15;69(2):185–9.
[22] Ku HH. Notes on the use of propagation of error formulas. Journal of Research of the National Bureau of Standards, Section C: Engineering and Instrumentation. 1966 Oct;70C(4):263.
[23] NCSS Statistical Software. Chapter 303: Deming Regression, [Internet]. Available from: https://www.ncss.com/wp-content/themes/ncss/pdf/Procedures/NCSS/Deming_Regression.pdf.